Micromechanical features of jet erosion - A numerical perspective

P. Cuéllar, L.-H. Luu, P. Philippe, F. Brunier-Coulin, N. Benahmed and S. Bonelli
IRSTEA, UR RECOVER, Aix-en-Provence, France

J.-Y. Delenne
UMR1208 IATE, INRA/CIRAD/Montpellier Supagro/Université de Montpellier, France

J. Ngoma
Institut Jean Lamour, CNRS - Université de Lorraine, Nancy, France

ABSTRACT: The erosion mechanisms driving the particle detachment of a soil under an impinging jet are here analysed from a micromechanical perspective combining the numerical Discrete Element and Lattice Boltzmann methods (DEM-LBM). Firstly, the local hydrodynamic conditions of both free and impinging jets are examined and briefly discussed, particularly on the relevance of the superficial irregularities of the granular assembly, which can dominate the local distribution of hydrodynamic variables over the impingement area. Profiles of both macromechanic and discrete (micromechanic) variables will be put forward. Then, the onset of erosion is reviewed from a topological point of view (locality of first grain motion) on the basis of a parametric study. Finally, the variation of the critical inflow velocity for the initiation of erosion in dependence on the particle size is also examined and briefly discussed.

1 INTRODUCTION

The earthen hydraulic civil constructions such as earth-dams and levees are often affected by a particular form of erosion caused by the flow of water over their surface, the so-called surface erosion (Foster et al. 2000). Other kinds of (internal) erosion such as piping, suffusion or contact erosion may also take place (Fell & Fry 2007), but involve different mechanisms and lie out of the scope of this paper. Several experimental procedures and devices have been developed for the general assessment of the sensitivity of granular materials like soils to the occurrence of surface erosion, among others the Jet Erosion Tests (JET) and the Hole Erosion Test (HET) (Hanson & Cook 2004; Benahmed & Bonelli 2012). The JET has received much attention and gained broad acceptance due to the relative simplicity of the experimental setup (Figure 1) and the possibility of performance of tests *in-situ* by means of portable JET devices (Hanson & Cook 2004).

The so-called erodibility parameters are widely used to quantify the likelihood and magnitude of the erosive degradation in terms of, on the one hand, the critical threshold of hydrodynamic shear stress (τ_c) for the initiation of erosion and, on the other hand, an erosion modulus (k_d) that relates the rate of material erosion to the hydrodynamic conditions at the eroded surface (Hanson & Cook 2004). A convenient and widely accepted form (though also controversial, see the recent discussion in Walder 2015) of

the erosion law can be then written in the following linear fashion:

$$E = k_d(\tau - \tau_c) \quad \text{for} \quad \tau > \tau_c \qquad (1)$$

where E is the erosion rate and τ is the hydraulic shear stress. Therefore, the evolution of erosion is this way described in terms of solely one variable, the often elusive shear stress at the eroded surface, which is a quantity averaged over time and space that should represent the hydrodynamic conditions at the fluid-solid interface. This is of course a very rough simplification of the complex conditions at the surface under an impinging jet, where actually the shear stress should be zero right at the stagnation point.
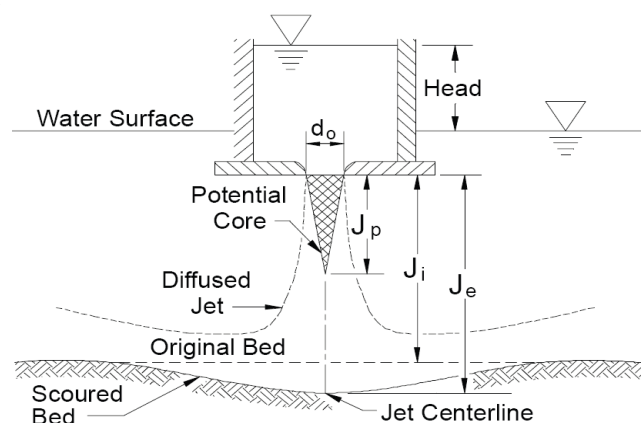

Figure 1. Conceptual sketch and relevant magnitudes of the Jet Erosion Test, taken from (Hanson & Cook 2004).

The aim of this paper is therefore to provide an insight into the local hydrodynamic conditions at the onset of jet erosion from a micromechanical perspective. For this purpose, an efficient numerical model that considers the fluid-solid interactions at the micro-scale (see also Cuéllar et al. 2015) is here introduced. Then, the local hydrodynamic variables at the surface are examined and the results from a preliminary parametric study varying the grain size and the jet's inflow velocity are discussed.

2 NUMERICAL TECHNIQUES

The approach adopted here combines the computational efficiency of the Lattice Boltzmann Method (LBM) for the fluid analysis with the relative simplicity of the Discrete Element Method (DEM) for the consideration of the solid particles. The field of applications of this combined technique already covers a wide spectrum of geomechanical problems (see e.g. Mutabaruka et al. 2014, Sibille et al. 2015, Ngoma 2015).

2.1 Fluid dynamics

The fluid dynamics are described here by means of a two-dimensional scheme of the lattice Boltzmann method, namely the so-called D2Q9, which is an explicit finite difference scheme of the continuous Boltzmann equation (Succi 2001, Lallemand & Luo 2003). The LBM involves the definition of a Cartesian lattice grid in the space and a discrete set of probability density functions and velocities of fluid particles at each grid point. The fluid dynamics arise then as the result of two basic steps: the collision and advection of the fluid particles following a set of rules aiming to ensure the conservation of mass, momentum and energy (i.e. the incompressible Navier-Stokes behaviour). However, some restrictions apply and this scheme only holds for very low Mach numbers, i.e. when fluid velocity is much lower than the lattice speed. All in all, the fluid phase is fully defined by specifying a lattice grid size Δx and a lattice speed c_s, the components s_α of the diagonal relaxation matrix S (inverse of the different relaxation times) and the fluid material parameters of density ρ_f and kinematic viscosity v. Further details of the employed formulation (multi-relaxation time type) can be found in (Cuéllar et al. 2015) and in the references contained therein.

2.2 Solid mechanics

The solid phase is introduced here by means of a discrete element model of the granular soil based on the classical Molecular Dynamics method pioneered by Cundall & Strack (1979). This way, the soil is represented by a two-dimensional assembly of circular particles accounting for the soil grains, whose trajectories are computed by simple integration of Newton's equations of motion. A great number of modifications of the smooth inter-particle contact and friction laws of the original model have been proposed in the past, in particular concerning the introduction of cohesive interactions between particles (see e.g. Delenne et al. 2004, Richefeu 2005, Jiang et al. 2013). Here, and for the sake of concision, only the rheological mechanisms for the description of a frictional granular material without cohesion will be considered, while the more complex case of a granular material with inter-particular cohesive bonds will be discussed in a forthcoming publication.

The interaction between two particles is thus formulated in terms of an interaction force F and an interaction moment M applied at their common contact point. The interaction force is thereby decomposed into its normal and shear components, F_n and F_s respectively, corresponding to the normal and tangential directions at the contact. The normal force F_n is here described in terms of the local interpenetration δ_n by means of a classical Kelvin-Voigt viscoelastic relationship defined by the normal stiffness and damping coefficients, k_n and η_n. On the other hand, the shear force arising at the frictional (non-cohesive) contact is defined here by a viscous-regularized Coulomb law (Richefeu et al. 2008, Schaefer et al. 1996) characterized by the static friction coefficient μ and the viscous coefficient of shear regularization k_s. This way, the shear force is computed in terms of the sliding velocity $\dot{\delta}_s$, which in practice does not preclude the consideration of static friction, since this variable never really vanishes. Due to the small time steps considered here (in the order of 10^{-6} s), the quasi-static equilibrium under static friction is reached in the short term through residual micro-slips. Finally, the interaction moment acting on each particle's centre is defined by the shear force with the particle's radius as lever arm and a rolling friction component that restrains the rolling motion of the particles (relative rotation without sliding). The latter can be described analogous to the shear friction in terms of the relative velocity of rotation, a rolling friction coefficient μ_ω and a coefficient of regularization k_ω (Richefeu 2005, McNamara 2011).

2.3 Solid-fluid coupling

The fluid-solid interaction, i.e. the coupling between the fluid and solid phases and the computation of the hydrodynamic forces on the discrete particles, is driven here by the momentum-exchange method proposed by Bouzidi et al. (2001), which relies on a generalized bounce-back rule for the fluid particles

and a linear interpolation strategy for arbitrary geometries in the LBM. On the other hand, the sub-cycling time integration technique proposed by Feng et al (2007) has been used to exploit the fact that the size of time steps required for the fluid computation is generally much larger than that necessary for the discrete solid phase. The number of DEM subcycles for each LBM step was nevertheless restricted to 2 in order to preserve the accuracy of the computed hydrodynamic forces on the solid particles. In order to overcome the inherent limitations imposed by the two-dimensionality to the fluid flow through a densely packed assembly of particles, a "hydraulic" geometrical reduction factor was employed matching the drag forces around a sphere to those of an equivalent cylinder with a reduced radius (Boutt et al. 2011, Cui et al. 2012).

3 JET HYDRODYNAMICS

Let us now examine the hydrodynamic conditions derived by the consideration of a free jet with prescribed fluid velocity at the injection nozzle (nozzle diametre b), and then observe the influence of introducing a granular surface perpendicular to the jet's axis and located at a distance H from the nozzle (see Fig. 2).
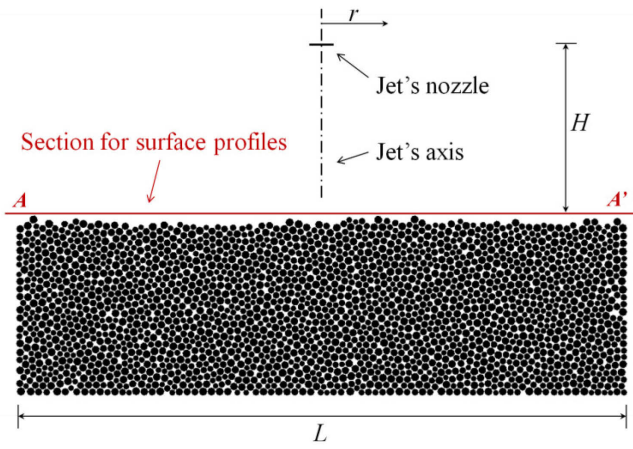

Figure 2. Spatial disposition of granular assembly, jet's nozzle and control section for fluid variables.

The arbitrary geometrical, material and rheological parameters employed for these simulations have been chosen either for convenience or based on usual values from the literature (see e.g. the comprehensive review in Luding 2008) and are summarized in Table 1. The corresponding flow may be described as an inertial laminar one (jet's Reynolds number $Re_j \sim 60$ to 100), i.e. a flow in the transition from a laminar to a turbulent regime.

3.1 Free jet conditions. Self-similarity

The particular case of a free jet, i.e. a fluid jet without obstacles, permits an implicit validation of the computational model by comparing the results to the analytical solutions of the Navier-Stokes equations proposed by several authors in the past (see for instance Bickley 1937 and Schlichting 1960 for the case of plane jets or Tritton 1988 for the general case of a round 3D jet). Such analytical models are based on the assumption of a self-similar propagation of the fluid jet and provide its centreline velocity u_m as follows (Badr 2014, Phares et al. 2000):

2D Poiseuille inlet: $u_m(h) = U_j \dfrac{(3/10)(5Re_j)^{1/3}}{((h+\lambda)/b)^{1/3}}$ (2)

2D uniform inlet: $u_m(h) = U_j \dfrac{0.454Re_j^{1/3}}{((h+\lambda)/b)^{1/3}}$ (3)

3D round, uniform jet: $u_m(h) = U_j \dfrac{(3/32)Re_j}{(h+\lambda)/b}$ (4)

where h is the axial distance to the jet's nozzle and λ is the nozzle distance to the virtual origin of the self-similar jet (Badr 2014).

The computed numerical results are a bit overly diffusive but nevertheless show a fair agreement with the analytical Poiseuille plane-jet solution (Figure 3) and lie, as expected, between the centreline velocity of the 2D uniform jet and that of the 3D round jet, which suffers a stronger decay of velocity due to the jet diffusion in all three dimensions.

Figures 4 and 5 show the computed velocity profiles perpendicular to the jet's axis, in a dimensional and normalised fashion respectively, confirming as well the hypothesis of self-similarity of the jet propagation. It can be noted that the velocity profile at the nozzle is here prescribed with the parabolic Poiseuille shape and it thus necessarily deviates from the self-similar shape where the other results collapse in the normalised diagram.

Table 1: Geometrical, material and model parameters for the presented simulations

| Solid phase		Fluid phase	
Particle mean size, D_{mean}	3×10^{-3} m	Jet's distance to surface, H	7×10^{-2} m
Polydispersity, D_{max} / D_{min}	1.5	Jet's nozzle size, b	5×10^{-3} m
Length of granular sample, L	2.63×10^{-1} m	Kinematic fluid viscosity, v	5×10^{-5} m²/s
Height of granular sample, H_s	8×10^{-2} m	Fluid density, ρ_f	847 kg/m³
Particle density, ρ_s	2230 kg/m³	Lattice grid size, Δx	2.3×10^{-4} m
Normal contact stiffness, k_n	1.1×10^5 N/m	Lattice speed, c_s	10 m /s
Shear contact stiffness, k_s	1.1×10^5 N/m	Hydraulic radius factor, R_h	0.8
Rolling stiffness, k_ω	$0.1 \times k_n$	Inlet fluid velocity, u_j	(0.45-0.8) m/s
Friction coefficients, $\mu=3\cdot\mu_\omega$	0.3		
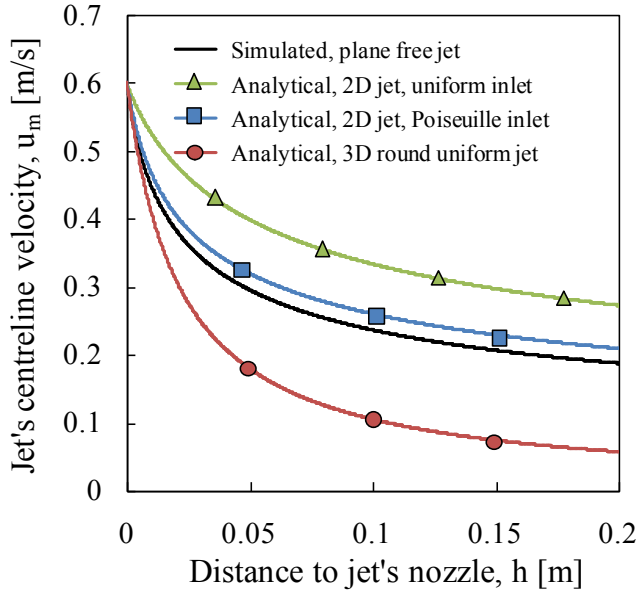
Figure 3. Centreline fluid velocity of a free jet. Comparison of numerical results (black solid line) with the analytical solutions for a 2D jet with uniform inlet (green triangles), a 2D jet with Poiseuille inlet (blue squares), and a 3D round jet (red circles).
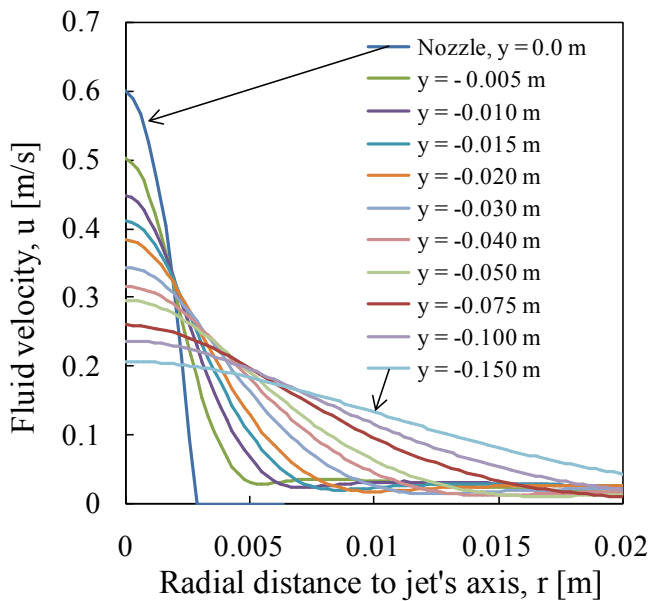
The variable adopted for normalisation of the radial distance is here the velocity half-width b_u proposed by Schlichting (1960):

$$b_u/h = 3.20 Re_j^{-2/3}(h/b)^{-1/3} \qquad (5)$$

3.2 Impingement on a fixed granular surface

Now let us proceed with the introduction of a solid fixed (non-erodible) wall with an irregular surface (granular profile) at a certain distance H from the jet's nozzle and perpendicular to its axis. Figure 6 shows the fluid velocity field and the jet's deflection at the solid surface. The flow is confined between the solid surface and the upper, closed boundary, while the lateral boundaries have been left open, and so the appearance of two convective cells can be observed.
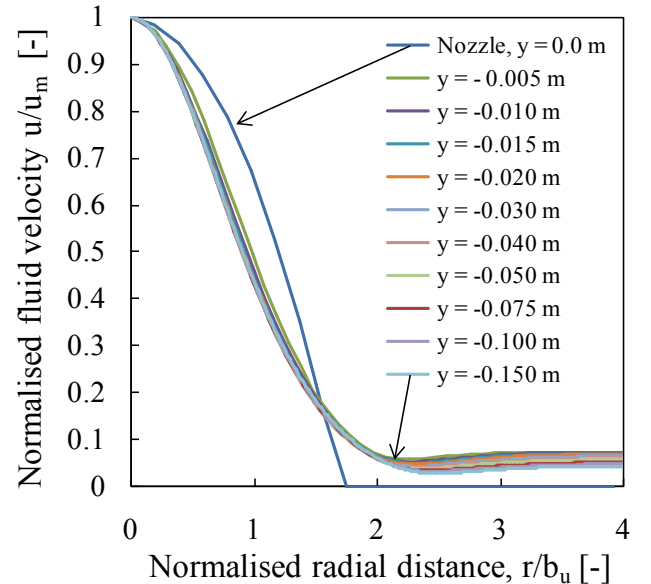

Figure 5. Normalised profiles of fluid velocity of a free jet. Basis for normalisation in the ordinates and abscissae are the centreline velocity $u_m(h)$ and the velocity half-width $b_u(h)$ respectively.

Figure 4. Horizontal profiles of fluid velocity of a free jet at several heights (reference: height of nozzle at $y=0$).

A closer inspection of the centreline velocity (Figure 7) shows now the appearance of a stagnation point (zero velocity) right at the solid surface and its consequent modification of the velocity axial profile, in fair agreement with the experimental trend derived by Beltaos & Rajaratnam (1977) for the jet velocity close to a solid wall, valid for ($0.75 \leq h/H \leq 1$):

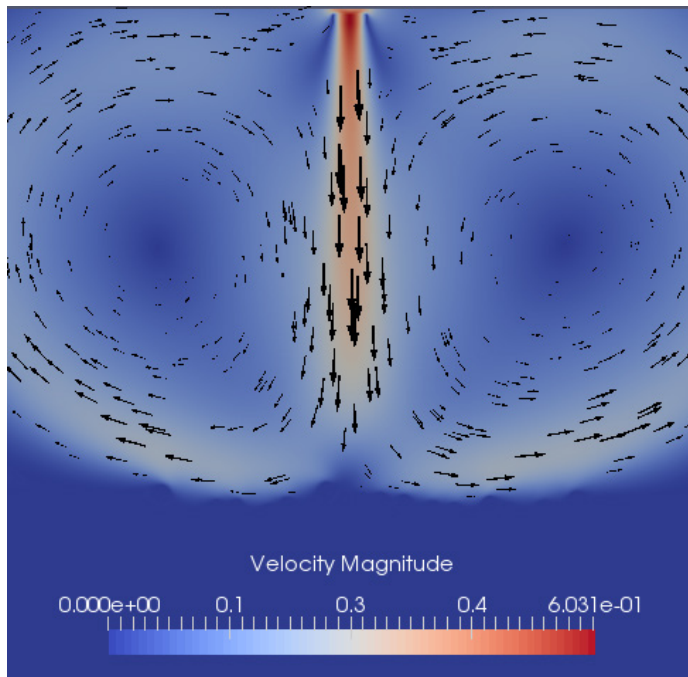$$u_m(h) = 5.5 U_j \sqrt{1 - h/H} \sqrt{b/H} \qquad (6)$$

Figure 6. Fluid velocity field of the jet's impingement on a fixed irregular surface. Arrow marker size is proportional to the velocity magnitude at each point.
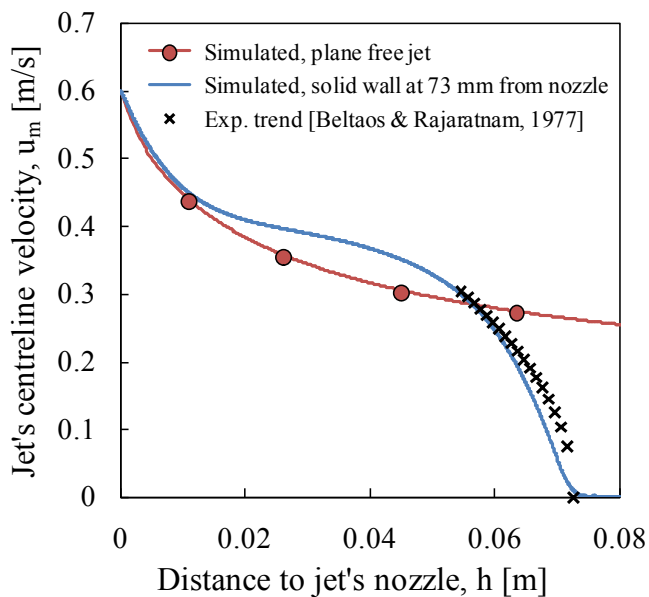

Figure 7. Computed centreline velocity of an impinging jet as compared to the free jet (red circles) and the experimental trend derived in (Beltaos & Rajaratnam 1977) (cross markers).

Now it is interesting to examine the profiles of fluid velocity, pressure and shear stress right over the solid surface, in particular taking into account the irregular profile of the granular assembly (Figure 8). The characteristic "M"-shape profile of fluid velocity with the stagnation point right under the jet's axis and its complementary maximum of fluid pressure can be appreciated in the figure. However, the maxima of shear stress, as well as the highest pressure gradients, are located actually right on the spots of the most prominent grains (the most exposed ones) of the irregular surface, marked with red circles in the lower diagram of Figure 8. Therefore, it appears that the topology of erosion, at least at its onset, can be dictated by the irregularities of the surface in the relevant impingement area, approximately in the range (-*H, H*) of radial distance from the jet's axis.

The employed numerical model has the advantage that it can provide access to a number of insightful micromechanical variables (i.e. at the grain scale). The lower diagram of Figure 9 shows the integrated hydraulic force acting specifically on each grain at the surface, while the upper diagram portrays the estimated maximum pressure gradients and shear stresses taking place directly around the solid particles (a refined calculation of these magnitudes is on course and shall be published in due time). It can be noted that the hydraulic force is obtained as the integral of the momentum exchange between fluid particles and the grain's surface (thus computed from an explicitly micromechanical point of view), whereas the pressure gradients and shear stresses are derived from macroscopic magnitudes of fluid pressure and velocity with a posterior identification of their maxima around the discrete particles. It seems therefore appropriate to highlight the apparent strong correlation between these three variables.
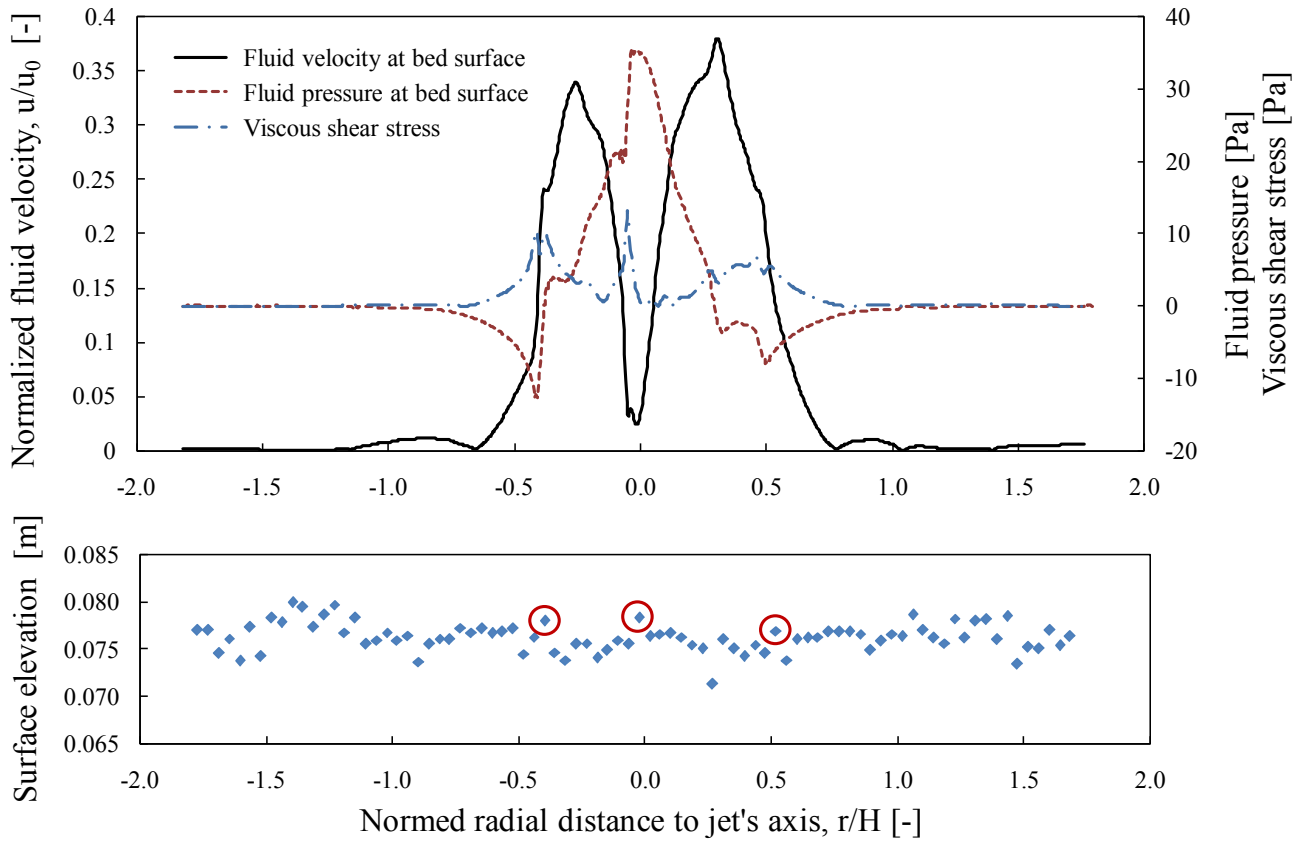
Figure 8. Upper diagram: Profiles of fluid velocity (solid line), pressure (red dashed) and shear stress (blue points and dashes) right above the granular surface. Lower diagram: Discrete profile of surface elevation of the granular assembly (prominent grains within the relevant impingement area highlighted with red circles). All profiles obtained at time t=8 s of the transient simulation.
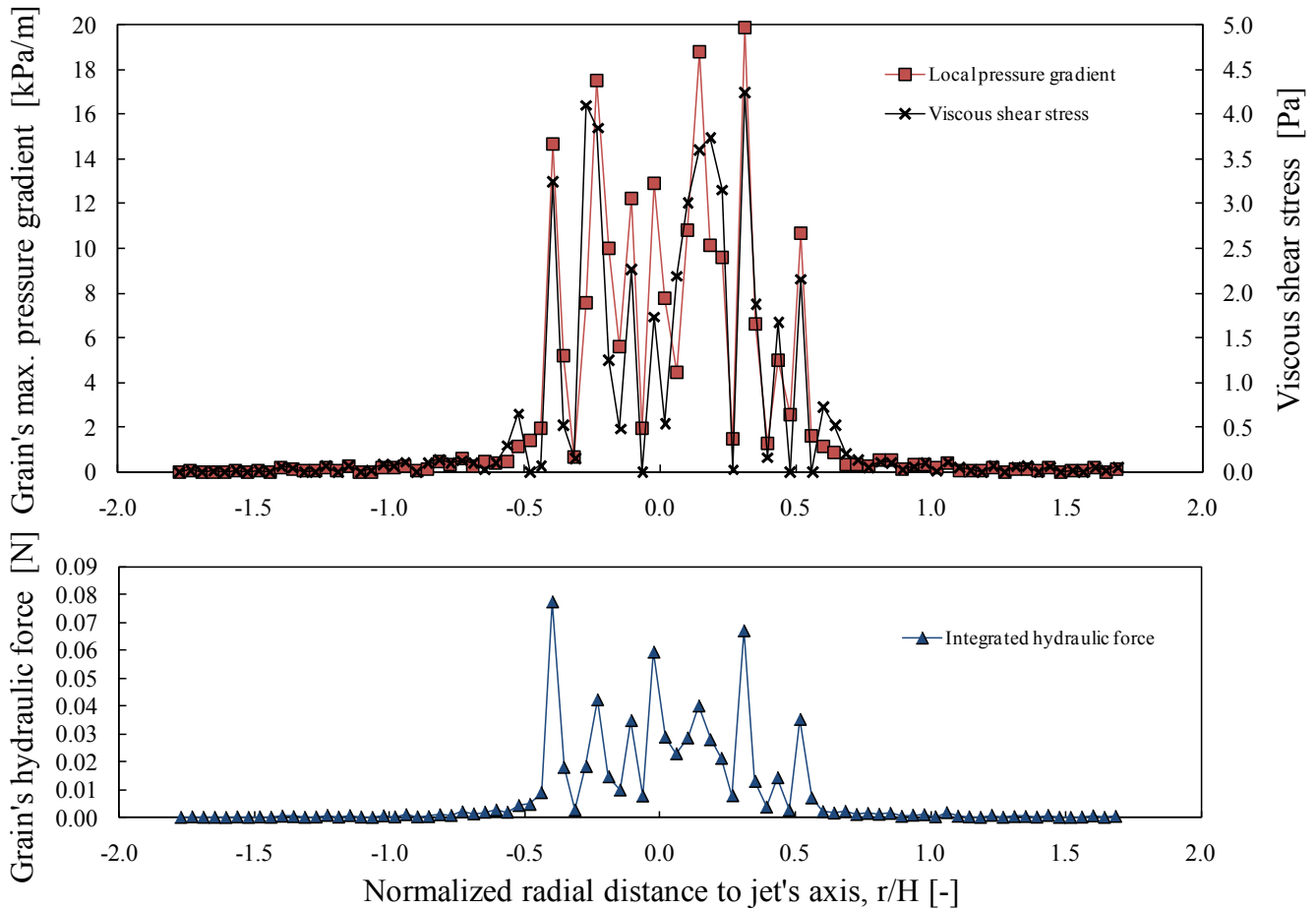

Figure 9. Upper diagram: Discrete profiles of maximum local pressure gradient (red squares) and shear stress (black cross markers) derived from macroscopic fluid variables around the surperficial grains. Lower diagram: Discrete profile of integrated hydraulic force at each grain on the surface of the assembly. All profiles obtained at time t=8 s of the transient simulation.

4 ONSET OF EROSION

4.1 Topology of first grain movement

Now let us turn the attention to the incipient motion of the soil grains under the action of the fluid jet when they are allowed to move. Figure 10 shows the topology of the first grain motion out of a parametric study encompassing three different random granular assemblies for each of four different mean particle sizes ranging from 1mm to 5mm, and two different fluid kinematic viscosities (4 x 10⁻⁵ and 5 x 10⁻⁵ m²/s respectively).

The inlet fluid velocity was kept constant with a Poiseuille profile and a maximum velocity of 0.6 m/s for all simulations. As a reference, Figure 10 also depicts the locations of the maxima of shear stress provided in (Rajaratnam 1976) and (Weidner et al. 2012) out of experimental and numerical analysis of the impinging jet respectively.

These results tend to show that the reference values of maximum shear stress can hardly predict the location of the motion onset which is rather governed by the irregularities of the surface, particularly as the size of the solid grains increases. In any case, the limitations of such a two-dimensional analysis may also play a relevant role in this respect. The superficial irregularities of a 2D granular assembly are in general more pronounced than in three-dimensional conditions, while the single grains at the surface resting on top of two other grains can in principle be set in motion more easily than their counterparts in 3D.
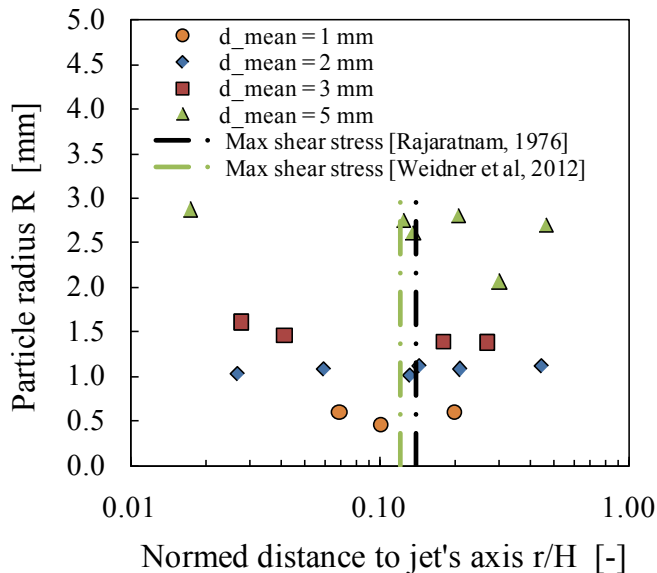

Figure 10. Initial location of the first particle to be displaced at the onset of jet erosion and reference locations of shear stress maxima out of (Rajaratnam 1976) and (Weidner et al. 2012).

4.2 Critical jet inflow velocity

Finally, the magnitude of the critical jet inflow velocity for the initiation of erosion has been addressed here by means of a further parameter variation. For this purpose, the parametric study introduced in Section 4.1 was repeated but this time featuring an increasing inflow velocity growing in time from an initial value of 0.45 m/s with a rate of 0,02 m/s².

Despite the relatively large error bars (standard deviations here), the general trend of growing critical velocity with particle size and decreasing fluid viscosity shown in Figure 11 seems plausible and also consistent with the experimental results obtained by Brunier-Coulin and coworkers (some preliminary details already available in Brunier-Coulin et al. 2015; 2016).
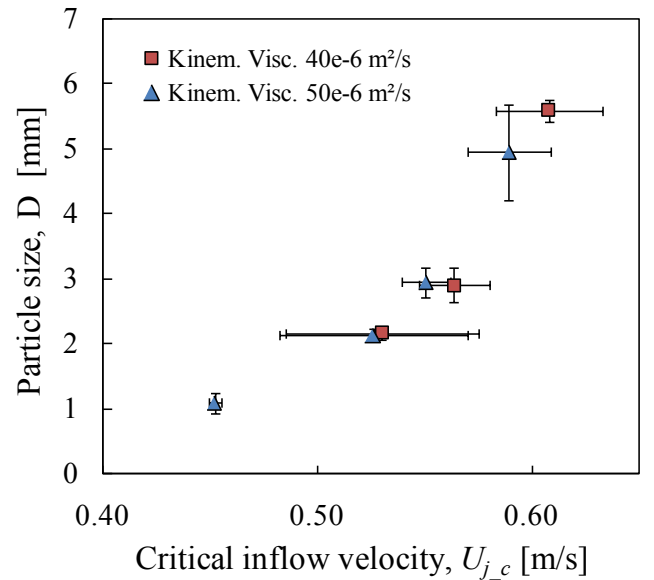

Figure 11. Critical jet velocity for the initiation of erosion in dependence of the solid particle size and of the fluid kinematic viscosity.

5 CONCLUSIONS AND OUTLOOK

The local distribution of hydrodynamic variables at the surface of a granular assembly under the action of an impinging jet can be suitably analysed from a micromechanical perspective employing a numerical model that combines the LBM and DEM techniques. The irregularities (rugosity) of the solid surface appear to bear a strong relevance on the distribution of shear stresses and pressure gradients, particularly as the size of the solid particles increases. The topology of the erosion onset seems therefore to be dictated by the granular profile and hardly follows the theoretical references of the maximum shear stress locality. Finally, the critical velocity of the jet for the initiation of erosion seems also to be relatively variable depending on the actual surface irregularities, but tends to show a seemingly consistent growth pattern with particle size.

The validity of these results is obviously constrained by the significant limitations imposed by the analytical method itself (i.a. the two-dimensionality, the particle size and shape, or the low Reynolds and Mach numbers, to name only a few) as well as by

the computational expense inherent to the multi-scale study case (a macroscopic problem featuring microscopic details). The presented model might nevertheless prove useful while providing a rare insight into the micromechanical origins of erosion.

The authors are presently working on further parametrical variations and an elaborate analysis of the micromechanical data for the case of jet erosion of frictional (non-cohesive) materials. On the other hand, a further study of granular assemblies with cohesion, thus allowing for tensile normal forces between the solid particles, is currently under way and shall complement the preliminary results already published in (Cuéllar et al., 2015).

ACKNOWLEDGEMENTS:

REFERENCES

Badr, S. 2014. Erosion d'un milieu granulaire par un jet. PhD thesis, Université Paris-Sud.

Benahmed, N.; Bonelli, S. 2012. Investigating concentrated leak erosion behaviour of cohesive soils by performing Hole Erosion Test. European Journal of Environmental and Civil Engineering, Vol. 16, n° 1, pp. 43-58.

Bickley, W.G. 1937. The plane jet. The London, Edinburgh and Dublin Philosophical Magazine and Journal Science, 23: 727–731

Boutt, D.F.; Cook, B.K. and Williams, J. R. 2011. A coupled fluid–solid model for problems in geomechanics:Application to sand production, Int. J. Numer. Anal. Meth. Geomech.35:997–1018x.

Bouzidi, M.; Firdaouss, M. and Lallemand, P. 2001. Momentum transfer of a Boltzmann-lattice fluid with boundaries, Phys. Fluids, Vol. 13, No. 11.

Brunier-Coulin, F.; Cuéllar, P. and Philippe, P. 2015. Mécanismes élémentaires de l'érosion d'un sol cohésif. In Proc. 22ème Congrès Français de Mécanique.

Brunier-Coulin, F.; Cuéllar, P. and Philippe, P. 2016. Local mechanisms of cohesive soil erosion. Submitted to 8th International Conference on Scour and Erosion, ICSE2016, Mathematical Institute, Oxford, UK..

Cuéllar, P., Philippe, P., Bonelli, S., Benahmed, N., Brunier-Coulin, F., Ngoma, J., Delenne, J.-Y., Radjai, F. 2015: Micromechanical analysis of the surface erosion of a cohesive soil by means of a coupled LBM-DEM model. Proc. 4th Int. Conf. on Particle-based Methods, PARTICLES 2015. E. Oñate, M. Bischoff, D.R.J. Owen, P. Wriggers & T. Zohdi (Eds).

Cui, X.; Li, J.; Chan, A. and Chapman, D. 2012. A 2D DEM–LBM study on soil behaviour due to locally injected fluid, Particuology10: 242– 252.

Cundall, P.A. and Strack, O.D.L. 1979. A discrete numerical model for granular assemblies, Géotechnique, Vol. 29, pp. 47-65.

Delenne, J.-Y.; El Youssoufi, M.S.; Cherblanc, F. and Bénet, J.-C. 2004. Mechanical behaviour and failure of cohesive granular materials,Int. J. Numer. Anal. Meth. Geomech., Vol. 28, pp. 1577–1594.

Fell, R., and Fry, J.-J. 2007. Internal Erosion of Dams and Their Foundations. Taylor & Francis, London.

Feng, Y.T.; Han, K. and Owen, D.R.J. 2007. Coupled lattice Boltzmann method and discrete element modelling of particle transport in turbulent fluid flows: Computational issues, Int. J. Numer. Meth. Engng. 72:1111–1134.

Foster, M., Fell, R., & Spannagle, M. 2000. The statistics of embankment dam failures and accidents. Can. Geotech. J. Volume 37:1000-1024.

Hanson, G.J. and Cook, K.R. 2004. Apparatus, test procedures and analytical methods to measure soil erodibility in situ. Engineering in Agriculture, ASAE, 20(4): 455-462.

Jiang, M.; Zhang, W.; Sun, Y. and Utili, S. 2013. An investigation on loose cemented granular materials via DEManalyses, Granular Matter15:65–84

Lallemand, P. and Luo, L.-S. 2003. Lattice Boltzmann method for moving boundaries, Journal of Computational Physics, Vol. 184, pp. 406–421.

Luding, S. 2008. Cohesive, frictional powders: contact models for tension, Granular Matter, Vol. 10, pp. 235–246.

McNamara, S. 2011. Molecular dynamics method, inDiscrete-element modeling of granular materials, Eds. Radjaï, F. and Dubois, F., Wiley-Iste

Mutabaruka, P.; Delenne, J.-Y.; Soga, K. and Radjai, F. 2014. Initiation of immersed granular avalanches, Phys. Rev. E. 89.

Ngoma, J. 2015. Etude numérique et expérimentale de la déstabilisation des milieux granulaires immergés par fluidisation, PhD thesis, Université d'Aix-Marseille.

Phares, D. J., Smedley, G. T., and Flagan, R. C. 2000. The wall shear stress produced by the normal impingement of a jet on a flat surface. J. Fluid Mech., 418, 351–375.

Richefeu, V. 2005. Approche par éléments discrets 3D du comportement de matériaux granulaires cohésifs faiblement contraints. PhD thesis. Université Montpellier II.

Richefeu, V.; El Youssoufi, M.S.; Peyroux, R. and Radjaï, F. 2008. A model of capillary cohesion for numerical simulations of 3D polydisperse granular media, Int. J. Numer. Anal. Meth. Geomech.,Vol. 32, pp. 1365–1383.

Schaefer,J.; Dippel, S. and Wolf, D. 1996. Force schemes in simulations of granular materials, Journal de Physique I, 6 (1), pp.5-20, EDP Sciences.

Schlichting, H. 1960. Boundary Layer Theory. McGraw-Hill.

Sibille, L.; Lominé, F.;Poullain, P.; Sail, Y. and Marot, D. 2015. Internal erosion in granular media: direct numerical simulations and energy interpretation, Hydrol. Process. 29(9), pp 2149–2163, Wiley and Sons.

Succi, S. 2001. The Lattice-Boltzmann Equation for fluid dynamics and beyond. Oxford university press, Oxford.

Tritton, D. J. 1988. Physical fluid dynamics. Oxford, Clarendon Press.

Walder, J. 2015. Dimensionless Erosion Laws for Cohesive Sediment. J. Hydraul. Eng., Volume 142, Issue 2.